



PAPER • OPEN ACCESS

Path integral Monte Carlo method for the quantum anharmonic oscillator

To cite this article: Shikhar Mittal *et al* 2020 *Eur. J. Phys.* **41** 055401

View the [article online](#) for updates and enhancements.

You may also like

- [ECoPANN: A Framework for Estimating Cosmological Parameters Using Artificial Neural Networks](#)
Guo-Jian Wang, Si-Yao Li and Jun-Qing Xia
- [ESTIMATING THE PROPERTIES OF HARD X-RAY SOLAR FLARES BY CONSTRAINING MODEL PARAMETERS](#)
J. Ireland, A. K. Tolbert, R. A. Schwartz et al.
- [Detecting Variability in Massive Astronomical Time-series Data. III. Variable Candidates in the SuperWASP DR1 Found by Multiple Clustering Algorithms and a Consensus Clustering Method](#)
Min-Su Shin, Seo-Won Chang, Hahn Yi et al.

Path integral Monte Carlo method for the quantum anharmonic oscillator

Shikhar Mittal^{1,3} , Marise J E Westbroek^{1,2}, Peter R King²
and Dimitri D Vvedensky^{1,4} 

¹ The Blackett Laboratory, Imperial College London, London SW7 2AZ, United Kingdom

² Department of Earth Science and Engineering, Imperial College London, London SW7 2BP, United Kingdom

³ Department of Theoretical Physics, Tata Institute for Fundamental Research, Mumbai 400005, India

E-mail: d.vvedensky@imperial.ac.uk

Received 6 March 2020, revised 28 April 2020

Accepted for publication 8 June 2020

Published 12 August 2020



CrossMark

Abstract


The Markov chain Monte Carlo (MCMC) method is used to evaluate the imaginary-time path integral of a quantum oscillator with a potential that includes a quadratic term and a quartic term whose coupling is varied by several orders of magnitude. This path integral is discretized on a time lattice on which calculations for the energy and probability density of the ground state and energies of the first few excited states are carried out on lattices with decreasing spacing to estimate these quantities in the continuum limit. The variation of the quartic coupling constant produces corresponding variations in the optimum simulation parameters for the MCMC method and in the statistical uncertainty for a fixed number of paths used for measurement. The energies and probability densities are in excellent agreement with those obtained from numerical solutions of Schrödinger's equation. The theoretical and computational framework presented here introduces undergraduates to the path integral formulations of quantum mechanics in real time and the partition function in statistical mechanics in imaginary time. The example of the anharmonic oscillator helps to build an intuition about the MCMC method of evaluating the partition function, which can then be used to solve other problems in physics and beyond.

⁴ Author to whom any correspondence should be addressed.



Original content from this work may be used under the terms of the [Creative Commons Attribution 4.0 licence](https://creativecommons.org/licenses/by/4.0/). Any further distribution of this work must maintain attribution to the author(s) and the title of the work, journal citation and DOI.

Keywords: path integral, imaginary time, quantum mechanics, anharmonic oscillator, Markov chain Monte Carlo method

 Supplementary material for this article is available [online](#)

(Some figures may appear in colour only in the online journal)

1. Introduction

The harmonic oscillator, one of the few exactly solvable quantum mechanical systems, is a mainstay of the undergraduate physics curriculum. Solutions for the energy eigenvalues and wave functions are obtained either by the analytic solution of the time-independent Schrödinger equation in terms of Hermite polynomials, or through a more abstract algebraic procedure based on raising and lowering operators [1]. An altogether different approach uses Heisenberg's matrix formulation of quantum mechanics [2, 3]. Although not a standard part of undergraduate quantum physics courses, Heisenberg's method, with suitable supplementary material [4], has pedagogical merit.

The operator method makes a direct connection to the statistics of bosons, a conceptual building block of modern physics. The bosonic character of the quantum harmonic oscillator is used in the quantization of small-amplitude vibrations in molecules and solids, the latter leading to phonons [5], the quantum theory of radiation [6–8], quantum field theory [9], and as an illustration of the correspondence principle [10]. Such diverse applications attest to the pivotal role of the harmonic oscillator in the conceptual and computational development of quantum physics.

Sufficiently small fluctuations in any system around a stable equilibrium point may be described in terms of decoupled harmonic oscillators (normal modes), regardless of the shape of the confining potential. However, there are regimes where the harmonic oscillator paradigm breaks down. For example, during the thermal expansion of solids, the transformations between solid phases, and chemical reactions, the displacements of atoms from their equilibrium positions cannot be regarded as small. As harmonic interactions are derived by truncating the Taylor series expansion of the interatomic potential at second order [5], we look to higher-order terms to augment the interaction potential. A basic one-dimensional model that incorporates the leading (quartic) correction to the harmonic potential has the Schrödinger equation,

$$\hat{H}\psi = \left(-\frac{\hbar^2}{2m} \frac{d^2}{dx^2} + \frac{m\omega^2 x^2}{2} + \lambda x^4 \right) \psi = E\psi, \quad (1)$$

in which m is the mass of the particle, $\omega = (k/m)^{1/2}$ is the natural frequency of the harmonic oscillator, where k is the stiffness of the potential, and λ is the coupling constant for the quartic term of the potential.

In the absence of an elementary analytic method for obtaining solutions of equation (1), attention turned to various approximate calculations. In Rayleigh–Schrödinger perturbation theory, the ground-state energy $E_0(\lambda)$ of equation (1) has the formal expansion

$$E_0(\lambda) = \frac{1}{2}\hbar\omega + \hbar\omega \sum_{n=1}^{\infty} A_n \left(\frac{\lambda\hbar}{m\omega^2} \right)^n, \quad (2)$$

where the expansion coefficients A_n must be determined. Bender and Wu calculated [11] these coefficients to 75th order and found a rapid increase in $|A_n|$, which suggests that (2)

diverges. In fact, they showed that this series diverges for any $\lambda > 0$ because of the singularity at $\lambda = 0$ that separates the regions where (1) has an infinite sequence of bound states ($\lambda > 0$) from the region where there are only metastable states that can escape to infinity ($\lambda < 0$) [11–13]. This explanation is a particular case of an argument first advanced by Dyson [14] for perturbation expansions in quantum electrodynamics. The divergence of the expansion (2) has provided the impetus for alternative perturbation expansions [15], resummation methods [16], and other computational schemes [17–19] for quantum anharmonic oscillators. Among these, the Wentzel–Kramers–Brillouin (WKB) method [1], which can be derived as a semi-classical approximation to the Feynman path integral [20–22], is particularly effective at producing accurate estimates for the eigenvalues of the quartic oscillator and other potentials [18].

In this paper, we adopt a somewhat different approach to solving equation (1) by evaluating the imaginary-time path integral for this system using the Markov chain Monte Carlo (MCMC) method [24]. Calculations are carried out on lattices with decreasing spacing to estimate the energy and probability density of the ground state and energies of low-lying excited states in the continuum limit. Comparisons with numerical integrations of Schrödinger’s equation demonstrate the accuracy of our approach. These calculations are also pedagogical: the wide range of λ -values in equation (1) used in this study help to develop an intuition about how the potential affects parameters and convergence. Although we are studying a specific case, the MCMC method can be applied to a quantum mechanical particle in any of the standard one-dimensional potentials [23–25] with minimal change to the basic procedure described here. In fact, the method can be generalized to systems with more degrees of freedom by adding more variables to the simulation [24, 26]. Imaginary-time time path integrals can also be formulated for classical statistical dynamics [27–30], as well as providing a bridge to quantum field theory [31].

Our evaluation of the path integral for the quantum anharmonic oscillator has been developed with undergraduates in mind. We have provided a concise derivation of the Feynman path integral for quantum mechanics and its imaginary-time counterpart as the partition function of statistical mechanics. The numerical evaluation of the imaginary-time path integral for the anharmonic oscillator illustrates how the strength of the anharmonic coupling constant affects the convergence of the MCMC method to the continuum limit. These calculations have been carried out to establish an intuitive understanding of how the MCMC method is applied to a particular system, with a view to applications to other systems. The discussion in section 5 provides several avenues for further applications that can be used as basis for projects, independent study, or even research.

The organization of this paper is as follows. We briefly outline the derivation of real-time and imaginary-time path integrals in section 2, referring to our earlier work [32]⁵ for a more comprehensive discussion. The MCMC method is summarized in section 3, and in section 4 we discuss how varying the coupling constant of the quartic term in the potential energy affects the parameters in this method. Section 5 presents the correlation functions that can be calculated from the imaginary-time formalism to obtain the energy eigenvalues of (1). We have calculated the energy and probability density of the ground state and the energies of the first two excited states. We summarize our results and discuss other applications of imaginary-time path integrals in section 5. Derivations, background material, and computer programs are provided in are provided in the supplementary information.

⁵ Supplementary material (<https://stacks.iop.org/EJP/41/055401/mmedia>) for reference [32] at <https://doi.org/10.1119/1.5024926>.

2. Real-time and imaginary-time path integrals

2.1. Feynman path integral

The time-dependent Schrödinger equation,

$$i\hbar \frac{\partial \psi}{\partial t} = \hat{H}\psi, \quad (3)$$

for a Hamiltonian operator

$$\hat{H} = \frac{\hat{p}^2}{2m} + V(\hat{x}), \quad (4)$$

has the formal solution

$$\psi(x, t) = e^{-i\hat{H}t/\hbar} \psi(x, 0), \quad (5)$$

where the exponential factor is the evolution operator. The connection to Feynman's path integral is made through the matrix elements of the evolution operator between any two initial and final position eigenstates, which is known as the 'propagator'. In Dirac's bra-ket notation⁵,

$$\begin{aligned} \langle x_f, t_f | x_i, t_i \rangle &= \langle x_f | e^{-i\hat{H}(t_f - t_i)/\hbar} | x_i \rangle \\ &= \int [Dx(t)] \exp \left[-\frac{i}{\hbar} \int_{t_i}^{t_f} L(x(t)) dt \right], \end{aligned} \quad (6)$$

in which L is the *classical* Lagrangian corresponding to the Hamiltonian operator (4):

$$L(x(t)) = \frac{m}{2} \left(\frac{dx}{dt} \right)^2 - V(x(t)). \quad (7)$$

The notation $[Dx(t)]$ in equation (6) means that the integral includes all space-time paths (x, t) between (x_i, t_i) and (x_f, t_f) . The left-hand side of (6) is known as the 'propagator', which represents the probability amplitude of a point particle at spacetime point (x_i, t_i) reaching the spacetime point (x_f, t_f) . The right-hand side expresses this amplitude as the integration of all paths connecting the two points with a weight determined by the classical action $S = \int_{t_i}^{t_f} L(x(t)) dt$ for each path [33, 34].⁶ Hence, the name 'path integral'. Equation (6), which establishes the path integral representation of the propagator, is the celebrated Feynman-Kac formula [33, 34, 37].

2.2. Imaginary-time path integrals

An alternative formulation of path integrals uses imaginary time, where t is replaced by $-i\tau$ [35]. The imaginary-time path integral analogous to equation (6) is

$$\begin{aligned} \langle x_f, \tau_f | x_i, \tau_i \rangle &= \langle x_f | e^{-\hat{H}(\tau_f - \tau_i)/\hbar} | x_i \rangle \\ &= \int [Dx(\tau)] \exp \left[-\frac{1}{\hbar} \int_{\tau_i}^{\tau_f} L_E(x(\tau)) d\tau \right], \end{aligned} \quad (8)$$

⁶ Although often called the third way to quantum mechanics, after the Schrödinger and Heisenberg formulations, Feynman's path integral in fact has a largely forgotten antecedent. In 1924, which predates the fundamental papers of Schrödinger and Heisenberg, Gregor Wenzel [35] published a paper in which the formulas and interpretations of a path integral approach to quantum optics were presented in a manner similar to those adopted by Feynman. Thus, the third way to quantum mechanics could indeed be regarded as the first! [36].

in which the classical Euclidean⁷ ‘Lagrangian’ is

$$L_E(x(\tau)) = \frac{m}{2} \left(\frac{dx}{d\tau} \right)^2 + V(x(\tau)). \quad (9)$$

Just as for real times, the path integral in equation (8) is over all paths between the initial point x_i at time τ_i and the final point x_f at time τ_f . Equation (8) is the imaginary time analogue of the Feynman–Kac formula (6).

The connection to quantum statistical mechanics is obtained by setting $x_f = x_i$, $\tau_i = 0$ and $\tau_f = \hbar\beta$, where $\beta = 1/(k_B T)$, k_B is Boltzmann’s constant, and T is the absolute temperature. The integral over $x(\tau)$ yields the trace of $e^{-\beta\hat{H}}$, which is the canonical partition function:

$$\begin{aligned} Z &= \int \langle x | e^{-\beta\hat{H}} | x \rangle dx = \text{Tr} \left(e^{-\beta\hat{H}} \right) \\ &= \int [Dx(\tau)] \exp \left[-\frac{1}{\hbar} \oint_0^{\hbar\beta} L_E(x(\tau)) d\tau \right]. \end{aligned} \quad (10)$$

The completeness relation,

$$\sum_{n=1}^{\infty} |n\rangle \langle n| = 1, \quad (11)$$

for the orthonormal eigenkets $\hat{H}|n\rangle = E_n|n\rangle$, when used in the trace in equation (10), yields the canonical partition function of quantum statistical mechanics⁵:

$$Z = \sum_{n=0}^{\infty} e^{-\beta E_n}. \quad (12)$$

2.3. Correlation functions and propagators

The energies of the ground state and excited states of the quantum anharmonic oscillator are encoded in correlation functions that are expectation values of products of the position operator:

$$\langle \hat{x}(\tau_1) \hat{x}(\tau_2) \cdots \hat{x}(\tau_n) \rangle = \frac{1}{Z} \text{Tr} \left[e^{-\beta\hat{H}} \hat{x}(\tau_1) \hat{x}(\tau_2) \cdots \hat{x}(\tau_n) \right]. \quad (13)$$

The energy E_0 of the ground state can be obtained from the expectation of the Hamiltonian (1) which, in conjunction with the virial theorem [1], is expressed in terms of correlation functions of x as [24]

$$E_0 = m\omega^2 \langle \hat{x}^2 \rangle + 3\lambda \langle \hat{x}^4 \rangle. \quad (14)$$

⁷Imaginary time versions of quantum field theories in d spatial dimensions are called Euclidean because the imaginary time plays the same role as a spatial coordinate, so the theory is invariant under rotations in $d + 1$ -dimensional Euclidean space. For a historical review of Euclidean field theories, see Guerra 2005 Euclidean field theory arXiv:math-ph/0510087v1.

An alternative expression for the ground-state energy, more closely related to those for excited states derived below, is

$$-\frac{d \log Z}{d\beta} = E_0. \quad (15)$$

The correlation functions $\langle \hat{x}^n \rangle$ for $n = 2$ and 4 are, from equation (13),

$$\langle \hat{x}^n(\tau) \rangle = \frac{1}{Z} \text{Tr} \left[e^{-\beta \hat{H}} \hat{x}^n(\tau) \right]. \quad (16)$$

By writing

$$\hat{x}(\tau) = e^{\hat{H}\tau/\hbar} \hat{x}(0) e^{-\hat{H}\tau/\hbar}, \quad (17)$$

which is the imaginary time counterpart of the Heisenberg picture for the time-dependence of operators, again using (11), and taking the limit $\beta \rightarrow \infty$, we obtain

$$\langle \hat{x}^n(\tau) \rangle = \langle 0 | \hat{x}^n(0) | 0 \rangle. \quad (18)$$

which is the expectation value of \hat{x}^n in the ground state.

The two-point correlation function for calculating the first excited state is

$$\langle \hat{x}(\tau) \hat{x}(0) \rangle_c = \langle \hat{x}(\tau) \hat{x}(0) \rangle - \langle \hat{x}(\tau) \rangle \langle \hat{x}(0) \rangle, \quad (19)$$

where the subscript ‘c’ denotes cumulant, which in diagrammatic analysis correspond to a connected diagram. Again using equations (11) and (17), yields

$$G_2(\tau) \equiv \lim_{\beta \rightarrow \infty} \langle \hat{x}(\tau) \hat{x}(0) \rangle_c = \sum_{n=1}^{\infty} e^{-(E_n - E_0)\tau/\hbar} |\langle 0 | \hat{x} | n \rangle|^2. \quad (20)$$

Hence, the energy of the first excited state is obtained as

$$-\hbar \lim_{\tau \rightarrow \infty} \left[\frac{d \log G_2(\tau)}{d\tau} \right] = E_1 - E_0. \quad (21)$$

The second excited state is obtained from the four-point connected correlation function

$$\langle \hat{x}(\tau)^2 \hat{x}(0)^2 \rangle_c = \langle \hat{x}(\tau)^2 \hat{x}(0)^2 \rangle - \langle \hat{x}(\tau)^2 \rangle \langle \hat{x}(0)^2 \rangle. \quad (22)$$

By proceeding as above, we obtain

$$G_4(\tau) \equiv \lim_{\beta \rightarrow \infty} \langle \hat{x}(\tau)^2 \hat{x}(0)^2 \rangle_c = \sum_{n=2}^{\infty} e^{-(E_n - E_0)\tau/\hbar} |\langle 0 | \hat{x}^2 | n \rangle|^2. \quad (23)$$

The second excited state is, therefore, determined from

$$-\hbar \lim_{\beta \rightarrow \infty} \left[\frac{d \log G_4(\tau)}{d\tau} \right] = E_2 - E_0. \quad (24)$$

The probability density of the ground-state wave function is obtained by following the development of Creutz and Freedman [24]. The probability $P(x)$ of a particle being found between

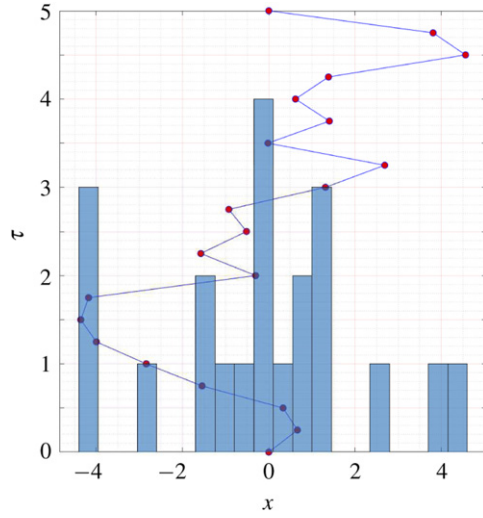


Figure 1. A discrete imaginary-time path between (0,0) and (0,5). The histogram indicates the number of times the particle crosses the corresponding spatial region.

positions $x - \frac{1}{2}\Delta x$ and $x + \frac{1}{2}\Delta x$ at any time t' in a real-time interval $[0, t]$ is given by the time-average

$$P(x) = \frac{1}{t} \int_0^t dt' \int_{x-\frac{1}{2}\Delta x}^{x+\frac{1}{2}\Delta x} dx' \frac{\langle x_f, t | x', t' \rangle \langle x', t' | x_i, 0 \rangle}{\langle x_f, t | x_i, 0 \rangle}, \quad (25)$$

The numerator in the integrand counts the paths that begin at $(x_i, 0)$, end at (x_f, t) , and pass through (x', t') for $0 \leq t' \leq t$. The propagator in the denominator counts all paths between $(x_i, 0)$ and (x_f, t) .

If Δx is assumed to be small enough so that the integral over x can be evaluated by keeping terms only to first order in Δx , we obtain

$$P(x) = \frac{\Delta x}{t \langle x_f, t | x_i, 0 \rangle} \int_0^t dt' \langle x_f, t | x, t' \rangle \langle x, t' | x_i, 0 \rangle. \quad (26)$$

The propagators are now written in terms of the eigenfunctions of \hat{H} by using the completeness relation (11):

$$\langle x', t' | x, t \rangle = \langle x' | e^{-i\hat{H}(t'-t)/\hbar} | x \rangle = \sum_{n=0}^{\infty} e^{-iE_n(t'-t)/\hbar} \psi_n^*(x') \psi_n(x). \quad (27)$$

By using this expression for each propagator in equation (26) and continuing to imaginary time $\tau = \hbar\beta$, the long-imaginary-time/low-temperature limit yields the probability density of the ground state:

$$P(x) = |\psi_0(x)|^2 \Delta x. \quad (28)$$

Figure 1 provides a schematic illustration of how the wave function is calculated by assigning a path along a time lattice to spatial bins with width Δx .

3. Markov chain Monte Carlo method

Monte Carlo simulations are carried out on a time lattice with N_τ time increments $\delta\tau$ with lattice points $x_n = n\delta\tau$ for $n = 0, 1, 2, \dots, N_\tau$. The n th time increment is $x_{n+1} - x_n$. Periodic boundary conditions are imposed on the lattice, whereby increment $N_\tau + 1$ equals increment 1. The imaginary-time path integral in equations (8) and (9) is the continuum limit of the discretized expression

$$\langle x_f | e^{-\hat{H}(\tau_f - \tau_i)/\hbar} | x_i \rangle = \lim_{N_\tau \rightarrow \infty} \int \prod_{k=1}^{N_\tau} dx_k \left(\frac{m}{2\pi\hbar\delta\tau} \right) e^{-S(\{x_k\})/\hbar}, \quad (29)$$

where $\{x_k\} \equiv x_1, x_2, \dots, x_{N_\tau}$, and

$$S(\{x_k\}) = \delta\tau \sum_{i=1}^{N_\tau} \left[\frac{m}{2} \left(\frac{x_{i+1} - x_i}{\delta\tau} \right)^2 + V(x_i) \right]. \quad (30)$$

We work with a dimensionless action. With each variable expressed in terms of a suitable power of the lattice spacing $\delta\tau$, we work in units where $\hbar = 1 = c$, and introduce the dimensionless variables

$$\tilde{m} = m\delta\tau, \quad \tilde{\omega} = \omega\delta\tau, \quad \tilde{x}_i = \frac{x_i}{\delta\tau}. \quad (31)$$

By combining equations (1), (30), and (31), the action for the anharmonic oscillator becomes

$$S(\{x_k\}) = \sum_{i=1}^{N_\tau} \left[\frac{\tilde{m}}{2} (\tilde{x}_{i+1} - \tilde{x}_i)^2 + \frac{\tilde{m}\tilde{\omega}^2 \tilde{x}_i^2}{2} + \tilde{\lambda} \tilde{m}^2 \tilde{\omega}^3 \tilde{x}_i^4 \right], \quad (32)$$

in which $\tilde{\lambda}$ is also dimensionless.

The MCMC method is based on determining the statistics of observables from paths (x_1, \dots, x_{N_τ}) that are representative of the distribution in equations (29) and (30). This requires generating reliable sequences of (pseudo) random numbers. We have used the Mersenne twister [41].

We begin with an initial path $P^{(0)}$, which may be an array of random numbers ('hot' start) or zeros ('cold' start). This path is updated by applying the Metropolis–Hastings algorithm [39, 40] to each element x_i of the path in random order, called a 'sweep'. There are two steps in the updating process:

- Generate a random number u from a uniform distribution in the interval $[-h, h]$, where h , called the hit size, must be chosen judiciously. If h is too large, few changes will be accepted; too small and the exploration of phase space will be slow. For the sets of simulations here, hit sizes were chosen to obtain an acceptance rate of 50%–60%.
- Propose the new value, $x_i' = x_i + u$, of the path element and calculate the resulting change ΔS in the action. New values that lower the action are always accepted, while those that would increase the action are accepted with probability $e^{-\Delta S}$.

One sweep produces the next path, e.g. $P^{(1)}$ from $P^{(0)}$. Each path is determined only by the immediately preceding path, so the complete sequence of paths forms a Markov chain, but the paths are correlated. The accuracy of the MCMC method relies on sampling from the distribution in equations (29) and (30) which, in turn, relies on the paths being stationary and independent. The initial path 'thermalizes', that is, attains equilibrium after N_{therm} sweeps. To counteract the inherent autocorrelation in a Markov chain, a number N_{sep} of paths between

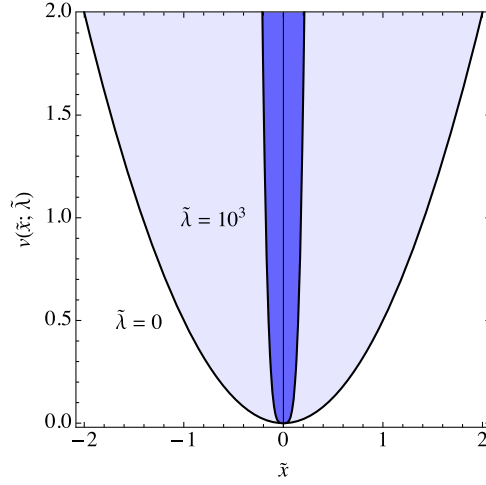


Figure 2. The potential $v(x; \lambda) = \frac{1}{2}\tilde{x}^2 + \tilde{\lambda}\tilde{x}^4$ for $\tilde{\lambda} = 0$, which is the potential for the harmonic oscillator (blue shading), and $\tilde{\lambda} = 10^3$, which corresponds to the strong quartic limit (blue shading). The quartic potential localizes the wave functions of the oscillators, which causes the corresponding energy eigenvalues to increase.

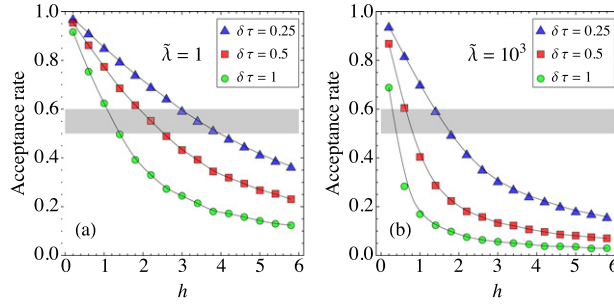


Figure 3. Acceptance rate versus the hit size h for the quantum anharmonic oscillator with quartic coupling constant (a) $\tilde{\lambda} = 1$ and (b) $\tilde{\lambda} = 1000$ for the indicated discretizations. The target of 50%–60% acceptance rate is indicated by shading. The curves are spline fits to the data.

successive paths used for measurements (i.e. representative of the equilibrium distribution) must be discarded. A detailed description of this process is provided in reference [32].

4. Parameters for MCMC simulations

For all calculations reported here, $\tilde{m} = \tilde{\omega} = \delta\tau$ and $N_\tau\delta\tau = 250$ in equation (32). Calculations have been performed for $\tilde{\lambda} = 0, 1, 50$ and 10^3 , which range from the harmonic oscillator to the strong quartic limit (figure 2). Such a large variation of $\tilde{\lambda}$ affects not just the quantum mechanical behavior of the oscillator, but also several parameters used in the MCMC method: the hit size h needed to achieve an acceptance rate of 50%–60%, and the number N_{sep} of paths that must be discarded between successive paths used for calculations. The coupling constant also affects the convergence to the continuum limit of the probability density of the ground state and the energy levels.

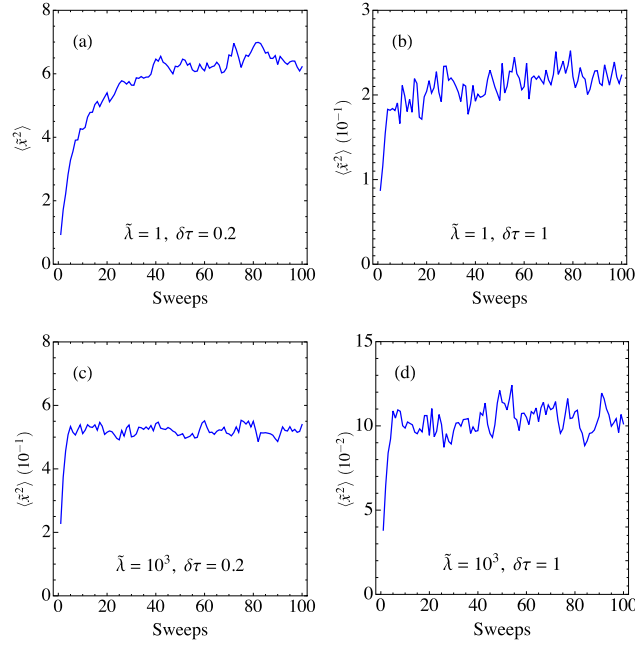


Figure 4. Equilibration of $\langle \tilde{x}^2 \rangle$ over the first 100 sweeps from the initial configuration for (a) $\tilde{\lambda} = 1$ and $\delta\tau = 0.2$, (b) $\tilde{\lambda} = 1$ and $\delta\tau = 1$, (c) $\tilde{\lambda} = 10^3$ and $\delta\tau = 0.2$, and (d) $\tilde{\lambda} = 10^3$ and $\delta\tau = 1$, with $N_{\tau}\delta\tau = 250$ for all simulations. Note the differences in the scales along the vertical axes.

Figure 3 compares the acceptance rate versus hit size for the anharmonic oscillator with weak ($\tilde{\lambda} = 1$) and strong ($\tilde{\lambda} = 10^3$) quartic coupling constants for several discretizations. These data were obtained as follows: (i) begin with a cold start and $h = 0.2$, (ii) ignore several initial sweeps, (iii) calculate the acceptance rate, as given in the pseudocode in reference [32], (iv) calculate the arithmetic mean of the acceptance rate for every 100 sweeps. The hit size is then increased by 0.2 and steps (i)–(iv) are repeated.

Most apparent in figure 3 is that, for each discretization, the target hit size is much smaller for the larger quartic coupling constant, which leads to larger changes in the action with increasing coupling and, thus, suppresses the acceptance rate. In other words, the exploration of phase space is slower, which is a natural consequence of the more localized potential associated with a stronger coupling constant (figure 2).

A key element of the MCMC method is the selection of paths used for calculations. These paths must be representative of the equilibrium distribution, as defined by the partition function, so the paths must first equilibrate from some initial configuration. The number N_{therm} of sweeps required to attain equilibrium is determined when the measured quantity fluctuates about a steady state, which depends on the observable, but generally increases as either $\delta\tau$ or $\tilde{\lambda}$ decreases. Typically, the equilibration of several observables is plotted and the maximum number of sweeps to equilibrium is used for all simulations.

Figure 4 shows the equilibration for $\langle \tilde{x}^2 \rangle$ for the anharmonic oscillator with coupling constants $\tilde{\lambda} = 1$ (a), (b) and $\tilde{\lambda} = 10^3$ (c), (d) for lattice spacings $\delta\tau = 0.2$ (a), (c) and $\delta\tau = 1$ (b), (d). Note the differences in scales of $\langle \tilde{x}^2 \rangle$ in each panel, which shows that the equilibrium value is much smaller for the system with the larger coupling constant. Also immediately apparent is

Table 1. The initial N_{therm} Metropolis–Hastings sweeps that are neglected and the hit size h , presented as (N_{therm}, h) , for the indicated discretizations $\delta\tau$ and coupling constants $\tilde{\lambda}$. For these simulations, N_{therm} and N_{sep} were of similar order of magnitude. No simulations were performed for values of $\tilde{\lambda}$ and $\delta\tau$ whose entry is indicated by a dash (-).

$\delta\tau$	$\tilde{\lambda} = 0$	$\tilde{\lambda} = 1$	$\tilde{\lambda} = 50$	$\tilde{\lambda} = 1000$
0.01	—	—	—	200, 16
0.02	—	—	300, 11	100, 14
0.05	—	500, 9	100, 9	100, 8
0.10	500, 5	200, 5	100, 5	100, 6
0.20	100, 4	100, 4	100, 3	100, 2
0.25	100, 3.5	100, 3.5	100, 2.5	100, 1.5
0.40	100, 2.5	100, 3.5	100, 1.6	100, 0.9
0.50	100, 2.5	100, 2	100, 1.3	100, 0.7
1.00	100, 1.5	100, 1.2	100, 0.5	100, 0.3

how many fewer sweeps from the initial path are required to attain equilibrium with increasing coupling constant.

The trends in figures 3 and 4 can be explained by the sharpening of the potential energy profile with increasing $\tilde{\lambda}$ (figure 2). All of our simulations began with cold starts. Thus, with increasing $\tilde{\lambda}$, the accessible configuration space decreases, so the attainment of equilibrium is correspondingly quicker. Similarly, the acceptance rate for a fixed hit size h is lower for larger $\tilde{\lambda}$ because of the increasing confinement near the origin at the expense of the classically forbidden region. This also explains why, for an observable such as $\langle \tilde{x}^2 \rangle$ (figure 4), sweeps over Markov chains show smaller fluctuations around their mean for larger $\tilde{\lambda}$. Finally, the increasing equilibrium value of $\langle \tilde{x}^2 \rangle$ with $\tilde{\lambda}$ is a direct result of the increasingly localized probability density of the ground-state wave function (section 5.1) caused by the sharpening potential energy profile (figure 2).

The number N_{sep} of sweeps discarded between successive measurements, and the hit size h for the discretizations $\delta\tau$ used for the calculations described in the following section are compiled in table 1. These entries were obtained from the data in figures 3 and 4 for each discretization and quartic coupling constant. The variations of simulation parameters in this table extends to other calculations using the MCMC method, such as the autocorrelation times and the application of the jackknife analysis for analyzing the statistics of correlated samples. All of our simulations began with cold starts, and we used 200 paths (every 100th sample out of a chain of 20 000) for all measurements. We used the method and code of reference [42] for estimating autocorrelation times and error analysis.

5. The quantum anharmonic oscillator

5.1. Probability density of the ground state

The properties of our Markov chains enable an indirect evaluation of the long-imaginary-time limit (32) of the expression (29) for the probability density of the ground state. In particular, the Markov chains in section 3, which are aperiodic, irreducible, and positively recurrent, guarantee not only that any initial chain approaches equilibrium, as the discussion accompanying figure 4 demonstrates, but that long-time limits may be replaced by ensemble averages (ergodicity) [25, 43].⁶

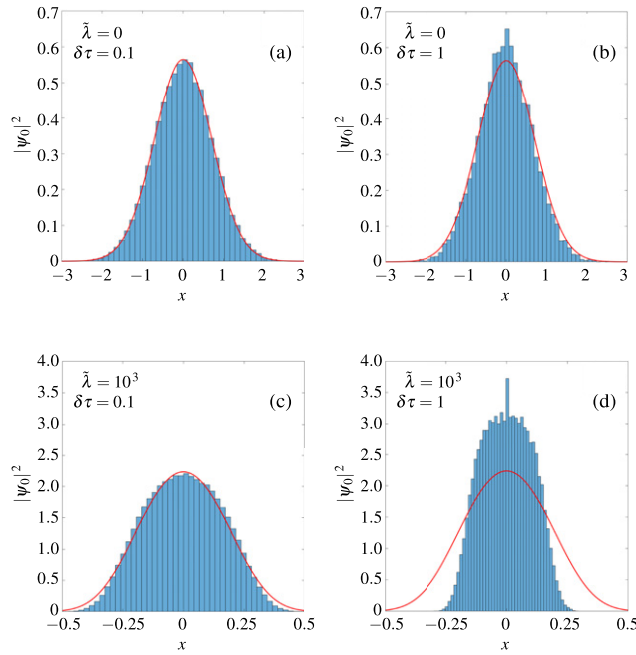


Figure 5. The probability densities $|\psi_0(x)|^2$ of the ground-state wave functions for the harmonic oscillator (a), (b) and the strong quartic limit (c), (d) in the Schrödinger equation with Hamiltonian (32) for $\delta\tau = 1$ (b), (d) and $\delta\tau = 0.1$ (a), (c). The histograms were obtained according to the procedure shown in figure 1, with 200 paths (every 100th from a chain of 20 000) used for determining the probability density. The red curves superimposed on these histograms are numerical solutions to Schrödinger's equations with the corresponding Hamiltonians (32) obtained by using the bvp4c solver of MATLAB (reference [44, 45]).⁴

Figure 5 shows the (normalized) probability densities $|\psi_0(x)|^2$ of the wave functions for the ground state of the Hamiltonian (32) with $\tilde{\lambda} = 0$, which is the harmonic oscillator, and with $\tilde{\lambda} = 10^3$, in which the quartic term dominates. The numerical integration of the corresponding Schrödinger equations⁴ is shown for comparison. Perhaps the most striking aspect of this figure is the enhanced localization of the wave function for $\tilde{\lambda} = 10^3$ compared with that for the harmonic oscillator ($\tilde{\lambda} = 0$). This is to be expected from the narrowing of the potential with increasing $\tilde{\lambda}$ (figure 1). Moreover, the rate of convergence to the continuum limit is considerably slower for the large quartic term. The errors for $\delta\tau = 1$ are small for the harmonic oscillator, but are substantial for the large quartic potential, with small discrepancies remaining in the tail of the distribution even for $\delta\tau = 0.1$.

5.2. Ground-state energy

The energies of anharmonic oscillators were expressed as correlation functions in section 2.3. The MCMC method necessitates evaluating discrete approximations to these quantities, which are then used to estimate the energies at decreasing lattice spacing $\delta\tau$. The results with the simulation parameters in table 1 are shown in figure 6 for $\tilde{\lambda} = 0, 1, 50$, and 10^3 . Also shown are the exact results [24, 30] for the harmonic oscillator (figure 6(a)) and spline fits⁴ to the data points for the anharmonic systems (figures 6(b)–(d)). The spline fits were used to estimate the

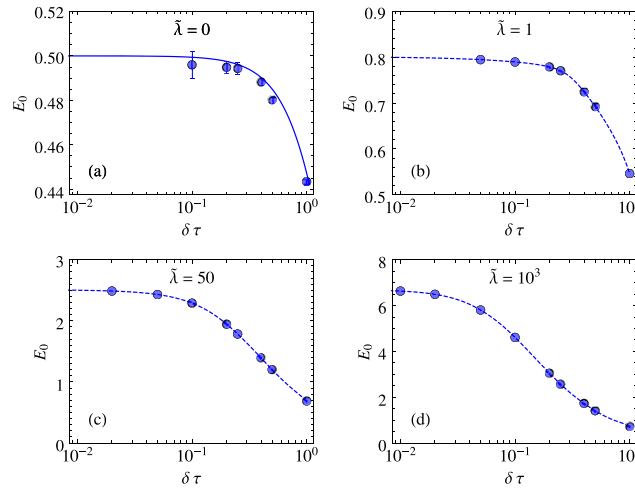


Figure 6. Calculation of the ground-state energy of the anharmonic oscillator with quartic couplings (a) $\tilde{\lambda} = 0$, (b) $\tilde{\lambda} = 1$, (c) $\tilde{\lambda} = 50$, and (d) $\tilde{\lambda} = 10^3$. The filled circles represent values calculated from the MCMC method. In (a), the solid line is the exact result calculated in reference [24, 30], while in (b)–(d), the broken curve is a (not-a-knot) cubic spline fit carried out on linear axes. The logarithmic axis for $\delta\tau$ is for presentation purposes only. Where error bars are not indicated, the errors are of the same size or smaller than the symbol.

Table 2. Ground-state energy of the anharmonic oscillator for the indicated values of $\tilde{\lambda}$. The column labelled MCMC is the data point in figure 6 with the finest discretization, spline is the value obtained by extrapolating the spline curve, SE is the energy obtained by the numerical integration of Schrödinger's equation, and the last column contains the energies calculated by the method in [17] for $\lambda > 0$.

$\tilde{\lambda}$	MCMC	Spline	SE	Ref. [17]
0	0.496	0.501	$\frac{1}{2}$	—
1	0.795	0.801	0.8038	0.8038
50	2.488	2.511	2.4998	2.4997
10^3	6.634	6.702	6.6941	6.6942

ground-state energies in the continuum limit on linear axes; the logarithmic axis for $\delta\tau$ is used in figure 6 for presentation purposes only.

The ground-state energies for the systems shown in figure 6 have been calculated by several methods, with the results compiled in table 2. The energies in the column labelled MCMC are obtained from the finest discretization in figure 6, while the column spline labels the energies extrapolated from the spline fits to the calculated data points. These two columns are the results obtained from the path integral method, either directly (MCMC) or inferred (spline). The remaining two columns contain essentially exact numerical results, obtained by the numerical integration of Schrödinger's equation⁴, and from the method of Hioe and Montroll [17], who used the Bargmann representation to develop rapidly converging algorithms for the energy levels of oscillators as a function of the anharmonic coupling constant.

The ground-state energy obtained from the extrapolation of the spline are within a few tenths of a per cent of the exact results. In contrast, the energies obtained from the path integral with

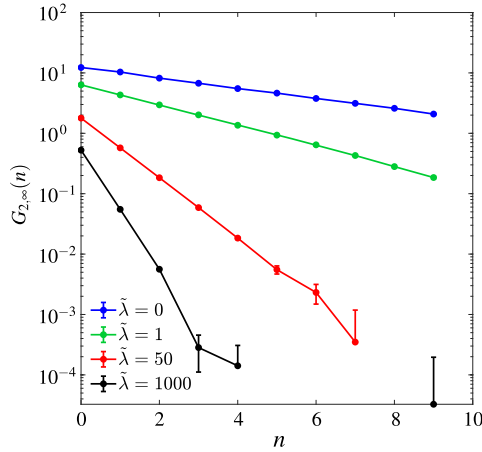


Figure 7. The asymptotic form of two-point correlation function in (34) for the indicated values of $\tilde{\lambda}$ for a lattice spacing of $\delta\tau = 0.2$. The slope for small values of n determine the difference $E_1 - E_0$ between the ground state and the first excited state.

the finest discretization show discrepancies by as much as 9%. This highlights the dual role of the spline fit: (i) as an estimate of the energy by extrapolation, and (ii) an indication of the improvement expected by reducing the time lattice spacing.

5.3. First excited state

The first excited of the anharmonic oscillator is obtained by evaluating the logarithmic derivative of the long-time limit of $G(\tau)$ in (20), which is the zero-temperature limit of the correlation function in (19). Equation (21) then establishes the difference $E_1 - E_0$ between the ground state and first excited state as the negative of the slope of $G(\tau)$ in the long- τ limit. On a time lattice, equation (21) is approximated as

$$\begin{aligned} -\frac{(E_1 - E_0)}{\hbar} &\approx \lim_{\tau \rightarrow \infty} \left\{ \frac{\log[G_2(\tau + \Delta\tau)] - \log[G_2(\tau)]}{\Delta\tau} \right\} \\ &= \lim_{\tau \rightarrow \infty} \left\{ \frac{1}{\Delta\tau} \log \left[\frac{G_2(\tau + \Delta\tau)}{G_2(\tau)} \right] \right\}. \end{aligned} \quad (33)$$

The approximate solution of this equation,

$$G_{2,\infty}(\Delta\tau) = G_{2,\infty}(0)e^{-(E_1 - E_0)\Delta\tau/\hbar}, \quad (34)$$

is independent of τ . As $\Delta\tau = n\delta\tau$ for some non-negative integer n , we can determine $E_1 - E_0$ by plotting $\log[G_{2,\infty}(n)]$ versus n . An example is shown in figure 7 for $\tilde{\lambda} = 0, 1, 50$, and 10^3 with $\delta\tau = 0.2$. The linear behavior, evident for small n , enables estimates to be made for E_1 , given the values of E_0 in table 2.

The calculation of the energy differences $E_1 - E_0$ are shown in figure 8 and the resulting energies of the first excited states are shown in table 3. The differences between estimates based on the extrapolation of the cubic spline and the exact values are of the order of 1% or less. However, the error bars for these calculations, particularly for $\tilde{\lambda} = 0$ and $\tilde{\lambda} = 1$, are much larger than the corresponding calculations of the ground-state energies (figure 6). Note,

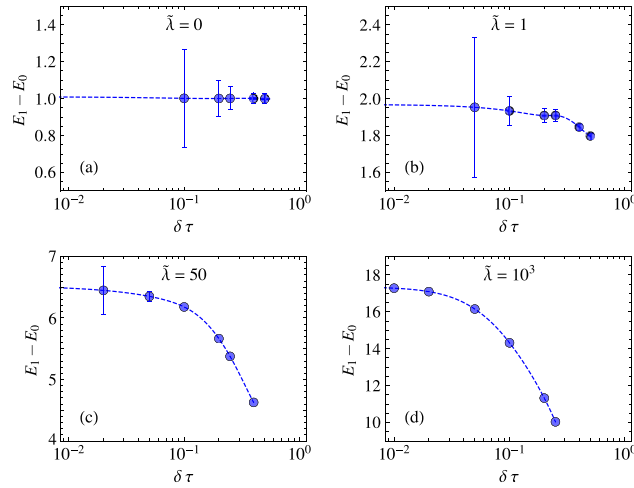


Figure 8. Calculation of the energy difference $E_1 - E_0$ of the anharmonic oscillator with quartic couplings (a) $\tilde{\lambda} = 0$, (b) $\tilde{\lambda} = 1$, (c) $\tilde{\lambda} = 50$, and (d) $\tilde{\lambda} = 10^3$. The filled circles represent values calculated from the MCMC method. The broken curves are a (not-a-knot) cubic spline fits carried out on linear axes. The logarithmic axis for $\delta\tau$ is for presentation purposes only. Where error bars are not indicated, the errors are smaller than the symbol size.

Table 3. Energy of the first excited state E_1 of anharmonic oscillators for the indicated values of $\tilde{\lambda}$. The first shows the energy differences $E_1 - E_0$ obtained from the extrapolation of the spline fits in figure 8. The column spline is E_1 obtained from extrapolating spline curves in figures 6 and 8, SE is E_1 obtained by the numerical integration of Schrödinger's equation, and the last column contains the energies calculated by the method in [17] for $\lambda > 0$.

$\tilde{\lambda}$	$E_1 - E_0$	Spline (E_1)	SE (E_1)	Ref. [17] (E_1)
0	1.010	1.511	$\frac{3}{2}$	—
1	1.969	2.770	2.7379	2.7379
50	6.523	9.034	8.9155	8.9151
10^3	17.368	24.069	23.9731	23.9722

in particular, that despite these large error bars, the mean of each calculation for the harmonic oscillator ($\tilde{\lambda} = 0$) is close to the exact value of 1.

5.4. Second excited state

The determination of the second excited state from (24) proceeds in a manner similar to that in the preceding section. The approximate solution analogous to equation (34) is

$$G_{4,\infty}(\Delta\tau) = G_{4,\infty}(0)e^{-(E_2-E_0)\Delta\tau/\hbar}, \quad (35)$$

where $G_{4,\infty}$ is the approximate solution of

$$-\frac{(E_2 - E_0)}{\hbar} \approx \lim_{\tau \rightarrow \infty} \left\{ \frac{1}{\Delta\tau} \log \left[\frac{G_2(\tau + \Delta\tau)}{G_2(\tau)} \right] \right\}. \quad (36)$$

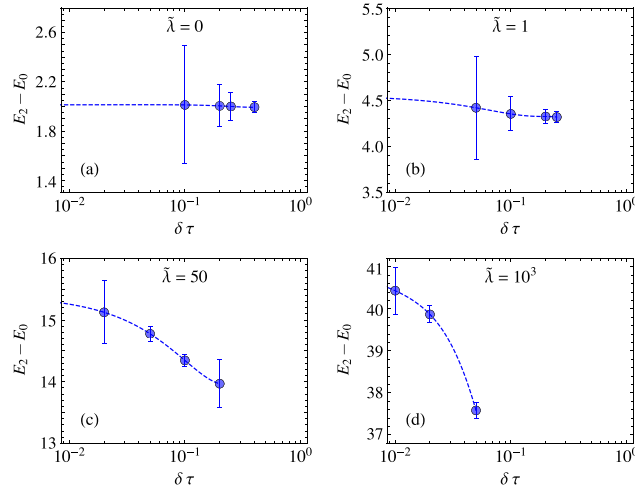


Figure 9. Calculation of the energy difference $E_2 - E_0$ of the anharmonic oscillator with quartic couplings (a) $\tilde{\lambda} = 0$, (b) $\tilde{\lambda} = 1$, (c) $\tilde{\lambda} = 50$, and (d) $\tilde{\lambda} = 10^3$. The filled circles represent values calculated from the MCMC method. The broken curves are a (not-a-knot) cubic spline fits carried out on linear axes. The logarithmic axis for $\delta\tau$ is for presentation purposes only. Where error bars are not indicated, the errors are smaller than the symbol size.

Table 4. Energy of the second excited state E_2 of anharmonic oscillators for the indicated values of $\tilde{\lambda}$. The first shows the energy differences $E_2 - E_0$ obtained from the extrapolation of the spline fits in figure 9. The column spline is E_2 obtained from extrapolating spline curves in figures 6 and 9, SE is E_2 obtained by the numerical integration of Schrödinger's equation, and the last column contains the energies calculated by the method in [17] for $\lambda > 0$.

$\tilde{\lambda}$	$E_2 - E_0$	Spline (E_2)	SE (E_2)	Ref. [17] (E_2)
0	2.014	2.515	$\frac{5}{2}$	—
1	4.551	5.352	5.1794	5.1793
50	15.400	17.911	17.4379	17.4370
10^3	40.904	47.606	47.0202	47.0173

and is again independent of τ . The energy difference $E_2 - E_0$ is obtained by plotting $\log[G_{4,\infty}(n)]$ versus n .

The results of such an analysis are shown in figure 9. The larger error bars for all of the oscillators are clearly evident, as is the more limited range of discretizations that are practical. Nevertheless, when estimates for $E_2 - E_0$ obtained from the extrapolation of the spline fits in figure 9 are combined with the corresponding values of E_0 in figure 6 are compared with exact calculations, our estimates are found to agree to within a few per cent (table 4).

6. Summary and extensions

We have applied the MCMC method to the evaluation of the imaginary-time path integral for the anharmonic oscillator with coupling strengths ranging from the harmonic limit to strongly quartic. Quantities calculated include the probability density of the ground state and the energies of the ground state and the first two excited states. The ground-state probability density

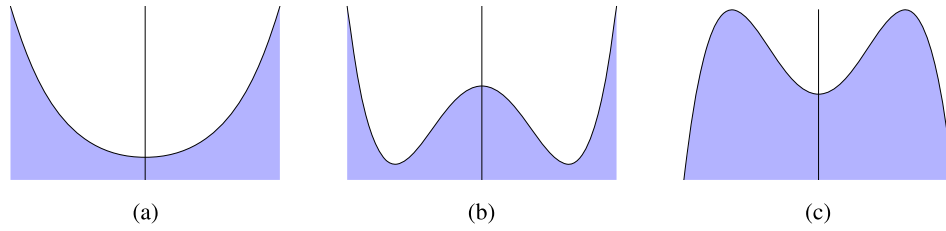


Figure 10. The profiles of potentials V in (1), written as $V(x) = rx^2 + \lambda x^4$, with (a) $r > 0$ and $\lambda > 0$, (b) $r < 0$, $\lambda > 0$, and (c) $r > 0$ and $\lambda < 0$.

becomes more localized as the potential becomes more localized due to the increase in the quartic coupling constant, and the energy levels increase accordingly, as expected from elementary quantum mechanics. Information about higher lying excited states becomes increasingly difficult to extract because they are exponentially suppressed in the imaginary-time path integral. Indeed, a comparison of figures 6, 8 and 9 illustrates how the statistical fluctuations become more pronounced away from the ground state for the same number of paths used for measurements.

The imaginary-time path integral formulation of many attractive features which suggest applications in condensed matter and other fields physics. The method we have used here, which is described in detail in references [23, 24, 32], can be applied to a single particle in a wide variety of potentials. Even the basic form (1) admits several qualitatively different types of potential (figure 10). With the potential written as $V(x) = rx^2 + \lambda x^4$, the potential in figure 10(a), which corresponds to $r > 0$ and $\lambda > 0$ is the type of potential used in this paper. As we have explained in the introduction, there are several methods available for the determining the ground and excited states of this potential, so our focus on this example is mainly the illustration of the path-integral Monte Carlo method. The potential in figure 10(b), with $r < 0$ and $\lambda > 0$, which is used as a model for tunnelling and bond formation in diatomic molecules, has been studied by Creutz and Freedman [24]. Finally, the potential in figure 10(c), which corresponds to $r > 0$ and $\lambda < 0$, has no bound states. The transition from (a) and (b), for which $\lambda > 0$, to (c), for which $\lambda < 0$, was used in the introduction to explain the divergence in the perturbation expansion in (2) because $\lambda = 0$ is a singular point that separates potentials with bound states from those with no bound states. The potentials in figures 10(b) and (c) are particularly interesting because quantum tunnelling can be problematic for semi-classical methods (such as WKB), in which case the numerical evaluation of the path integral becomes indispensable for establishing benchmarks.

An altogether different type of application of the path-integral Monte Carlo method is to quantum particles in confined systems. The interplay between interactions and particle exchange leads to many intriguing effects in systems of Bose and Fermi particles. Even one-dimensional or quasi-one-dimensional systems are of interest, including the behavior of electrons in quantum wires and carbon nanotubes, where electronic motion is allowed in one dimension, but strongly restricted in the two lateral dimensions. The harmonic potential can be used as a model of electrons (and holes) in semiconductor quantum dots and confined cold atoms. Extensions to multi-particle systems have also been considered, including superfluidity and Bose condensation in ^4He [46], and properties of interacting electrons in solids [47].

Moving away from physics, the path integral formalism has been applied to study the value of financial instruments known as options [48–50]. Path integrals admit several levels of solution, such as mean-field theory and steepest descent. The MCMC method provides the standard

against which the accuracy of these approximations is determined, as well as investigating the effect of lifting some of the basic assumptions of pricing models.

Finally, a word about projects. The present paper is based on the (postgraduate) MSc thesis of the principal author. But there have also been several undergraduate projects that have utilized the MCMC method guided by the presentation in [32]. Two final-year MSci (two-term) projects studied quantum particles confined to a two-dimensional square well based on their statistics, but without any interactions. Three final-year BSc (one-term) projects studied various financial instruments within the Black–Scholes framework and proceeded to investigate lifting some of the fundamental assumptions of the Black–Scholes model.

Acknowledgments

MJEW was supported through a Janet Watson scholarship from the Department of Earth Science and Engineering and a studentship in the Centre for Doctoral Training on Theory and Simulation of Materials funded by the EPSRC (EP/L015579/1).

ORCID iDs

Shikhar Mittal  <https://orcid.org/0000-0002-0247-618X>

Dimitri D Vvedensky  <https://orcid.org/0000-0002-4990-0208>

References

- [1] Merzbacher E 1998 *Quantum Mechanics* 3rd edn (New York: Wiley)
- [2] Heisenberg W 1925 Über quantentheoretische umdeutung kinematischer und mechanischer Beziehungen *Z. Phys.* **33** 879–93
Heisenberg W 1967 *Quantum-Mechanical Reinterpretation of Kinematic and Mechanical Relations (Sources of Quantum Mechanics)* ed B L van der Waerden (Amsterdam: North-Holland) pp 261–76 (Engl. Transl.)
- [3] Born M and Jordan P 1925 Zur quantenmechanik *Z. Phys.* **34** 858–88
Born M and Jordan P 1967 *On Quantum Mechanics (Sources of Quantum Mechanics)* ed B L van der Waerden (Amsterdam: North-Holland) pp 277–306 (Engl. Transl.)
- [4] Aitchison I J R, MacManus D A and Snyder T M 1972 Understanding Heisenbergs ‘magical’ paper of July 1925: a new look at the calculational details *Am. J. Phys.* **72** 1370–9
- [5] Ashcroft N W and Mermin N D 1976 *Solid State Physics* (Philadelphia, PA: Saunders)
- [6] Fermi E 1932 Quantum theory of radiation *Rev. Mod. Phys.* **4** 87–132
- [7] Bohm D 1989 *Quantum Theory* (New York: Dover)
- [8] Feynman R P, Leighton R B and Sands M 1963 *The Feynman Lectures on Physics* (Mainly Mechanics, Radiation, and Heat) vol 1 (Reading, MA: Addison-Wesley) ch 41
- [9] Zee A 2010 *Quantum Field Theory in a Nutshell* 2nd edn (Princeton, NJ: Princeton University Press)
- [10] Liboff R L 1984 The correspondence principle revisited *Phys. Today* **37** 50–5
- [11] Bender C M and Wu T T 1969 Anharmonic oscillator *Phys. Rev.* **184** 1231–60
- [12] Bender C M and Wu T T 1973 Anharmonic oscillator. II. A study of perturbation theory in large order *Phys. Rev. D* **7** 1620–36
- [13] Bender C M 1978 Perturbation theory in large order *Adv. Math.* **30** 250–67
- [14] Dyson F J 1952 Divergence of perturbation theory in quantum electrodynamics *Phys. Rev.* **85** 631–2
- [15] Halliday I G and Suranyi P 1980 Anharmonic oscillator: a new approach *Phys. Rev. D* **21** 1529–237
- [16] Simon B 1970 Coupling constant analyticity for the anharmonic oscillator *Ann. Phys.* **58** 76–136
- [17] Hioe F T and Montroll E 1970 Quantum theory of anharmonic oscillators. I. Energy levels of oscillators with positive quartic anharmonicity *J. Math. Phys.* **16** 1945–55
- [18] Bender C M, Olaussen K and Wang P S 1977 Numerological analysis of the WKB approximation in large order *Phys. Rev. D* **16** 1740–8

- [19] Banerjee K, Bhatnagar S P, Choudhry V and Kanwal S S 1978 The anharmonic oscillator *Proc. R. Soc. A* **360** 575–86
- [20] Dashen R F, Hasslacher B and Neveu A 1974 Nonperturbative methods and extended-hadron models in field theory. I. Semiclassical functional methods *Phys. Rev. D* **10** 4114–29
- [21] Rajamaran R 1975 Some non-perturbative semi-classical methods in quantum field theory (a pedagogical review) *Phys. Rep.* **21** 227–313
- [22] Holstein B R and Swif A R 1982 Path integrals and the WKB approximation *Am. J. Phys.* **50** 829–32
- [23] Lawande S V, Jensen C A and Sahlin H L 1969 Monte Carlo integration of the Feynman propagator in imaginary time *J. Comput. Phys.* **3** 416–43
- [24] Creutz M and Freedman B 1981 A statistical approach to quantum mechanics *Ann. Phys.* **132** 427–62
- [25] Morningstar C 2007 The Monte Carlo method in quantum field theory (arXiv:[hep-lat/0702020v1](https://arxiv.org/abs/hep-lat/0702020v1))
- [26] Lawande S V, Jensen C A and Sahlin H L 1971 He and H-1¹S and 2³S states computed from Feynman path integrals in imaginary time *J. Chem. Phys.* **54** 445–52
- [27] Pethica R 1977 The functional formalism of classical statistical dynamics *J. Phys. A: Math. Gen.* **10** 777–89
- [28] De Dominicis C and Peliti L 1978 Field-theory renormalization and critical dynamics above T_c : helium, antiferromagnets, and liquid-gas systems *Phys. Rev. B* **18** 353–76
- [29] Jensen R V 1981 Functional integral approach to classical statistical dynamics *J. Stat. Phys.* **25** 183–210
- [30] Westbroek M J E, King P R and Vvedensky D D 2018 Evaluation of the path integral for flow through random porous media *Phys. Rev. E* **97** 042119
- [31] Zinn-Justin J 2005 *Path Integrals in Quantum Mechanics* (Oxford: Oxford University Press)
- [32] Westbroek M J E, King P R, Vvedensky D D and Dürr S 2018 User's guide to Monte Carlo methods for evaluating path integrals *Am. J. Phys.* **86** 293–304
- [33] Feynman R P 1948 Space-time approach to non-relativistic quantum mechanics *Rev. Mod. Phys.* **20** 367–87
- [34] Feynman R P and Hibbs A R 1965 *Quantum Mechanics and Path Integrals* (New York: McGraw-Hill)
- [35] Wentzel G 1924 Zur quantenoptik (on quantum optics) *Z. Phys.* **22** 193–9
- [36] Antoci S and Liebscher D 1997 The third way to quantum mechanics is the forgotten first (arXiv:[physics/9704028v1](https://arxiv.org/abs/physics/9704028v1))
- [37] Kac M 1949 On distributions of certain Wiener functionals *Trans. Am. Math. Soc.* **65** 1–13
- [38] Brush S G 1961 Functional integrals and statistical physics *Rev. Mod. Phys.* **33** 79–92
- [39] Metropolis N, Rosenbluth A W, Rosenbluth M N, Teller A H and Teller E 1953 Equation of state calculations by fast computing machines *J. Chem. Phys.* **21** 1087–92
- [40] Hastings W A 1970 Monte Carlo sampling methods using Markov chains and their applications *Biometrika* **57** 97–190
- [41] Matsumoto M and Nishimura T 1998 Mersenne twister: a 623-dimensionally equidistributed uniform pseudo-random number generator *ACM Trans. Model. Comput. Simul.* **8** 3–30 . The period of the Mersenne twister is a Mersenne prime number, which has the form $2p - 1$, where p is also a prime number the standard implementation of the Mersenne twister $p = 19937$
- [42] Wolff U 2004 Monte Carlo errors with less errors *Comput. Phys. Commun.* **156** 143–53
- [43] Roberts G O and Rosenthal J S 2004 General state space Markov chains and MCMC algorithms *Probab. Surv.* **1** 20–71
- [44] MATLAB R2018a Update 3 (9.4.0.885841) (Natick: The MathWorks)
- [45] Kutz J N 2013 *Data-Driven Modeling & Scientific Computation: Methods for Complex Systems & Big Data* (Oxford: Oxford University Press)
- [46] Ceperley D M 1995 Path integrals in the theory of condensed helium *Rev. Mod. Phys.* **67** 279–355
- [47] Foulkes W M C, Mitas L, Needs R J and Rajagopal G 2001 Quantum Monte Carlo simulations of solids *Rev. Mod. Phys.* **73** 33–83
- [48] Linetsky V 1997 The path integral approach to financial modeling and options pricing *Comput. Econ.* **11** 129–63
- [49] Baaquie B E 2004 *Quantum Finance: Path Integrals and Hamiltonians for Options and Interest Rates* (Cambridge: Cambridge University Press)
- [50] Kleinert H 2009 *Path Integrals in Quantum Mechanics, Statistics, Polymer Physics, and Financial Markets* 5th edn (Singapore: World Scientific)